X-ray study of the intracluster medium of Abell 4038 with XMM-Newton

Author:
Geert RAAIJMAKERS

Supervisor:
Dr. Hiroki AKAMATSU
Dr. Anton VAN DE VEN

January 2015

Universiteit Utrecht

UTRECHT UNIVERSITY

Abstract

Faculty of Science

SRON Netherlands Institute for Space Research

Bachelor of Science

**X-ray study of the intracluster
medium of Abell 4038 with**

XMM-Newton

by Geert RAAIJMAKERS

The intracluster medium offers a detailed way of studying the metal enrichment in the Universe. An X-ray observation of Abell 4038, a rich cluster of galaxies, is made with XMM-Newton with an exposure time of 67 ks. After filtering the data from soft-proton flaring, the spectrum of the core region with radius $0.2 \times R_{500}$ is extracted. By fitting the background components and the cluster emission, the temperature and abundances of O, Ne, Mg, Si, S, Ar, Ca, Fe and Ni are obtained. With the abundances the ratio between type Ia and core-collapse supernovae is calculated and compared with other papers (e.g. de Plaa et al. 2007, Sato et al. 2007). The spectra of 7 concentric annuli are also extracted, resulting in the radial profiles for the temperature and the abundances of iron and silicium. The temperature profile indicates that A4038 is a cool-core cluster, and the centrally peaked abundances suggest that the cluster is in a relaxed state. Furthermore, a β-model is fitted through the radial profile of the surface brightness to obtain the core radius r_c. The small value of this radius is similar to that of other relaxed clusters, indicating again that A4038 is a relaxed cluster.

Acknowledgements

First of all, I would like to thank my direct supervisor dr. Hiroki Akamatsu for giving weekly feedback and answering all my questions. He guided me in the right direction by providing relevant papers and giving important insights. Secondly I would like to thank MSc. Francois Menier, for providing much help with the scripts for the data reduction and spectral analysis. I would also like to thank dr. Anton van de Ven, for checking the final written work, and Jelle de Plaa and Jelle Kaastra for making it possible to do my bachelor thesis at SRON.

Contents

Chapter 1

Introduction

Clusters of galaxies are the largest gravitationally bound objects in the Universe [1], forming through the merger of subclusters and groups [2]. Clusters consist of three main components, namely galaxies, intracluster medium (ICM) and dark matter. The mass of a cluster is around 10^{15} $M_\odot$, where $M_\odot$ is the solar mass, and have typical volumes of 100 Mpc^3. The dark matter makes up most of the clusters mass ($\sim$80 %), followed by the ICM ($\sim$16 %) and the galaxies ($\sim$4 %). This ICM is a hot (10^6-10^8 Kelvin) X-ray emitting gas filling up the spaces between the galaxies and is a useful tool to study clusters [3]. The X-ray emission from the plasma is due to three different radiation processes. The first one is called bremsstrahlung and occurs when a free electron has a close fly-by with an ion, thereby getting deflected and decelerated. The loss in kinetic energy is then converted in a photon and emitted. The second is recombination radiation, where a free electron is captured by an ion. The third is called deexcitation radiation and occurs when an electron changes quantum levels in an ion. The first two processes create a continuum radiation whereas the third process gives rise to line radiation [4]. Because of the low density of the plasma, with an electron density n_e of $10^{-4} - 10^{-2}$ cm^{-3}, most of the emitted X-rays do not interact between their emission in the plasma and their detection at the telescope. This gives a unique opportunity to study the ICM at different depths, instead of just at the surface as with stars for example [2]. The first measured X-ray spectrum with the satellite Ariel V indicated the presence of iron in the ICM, by detecting highly ionized Fe-K line emission [5]. When the ASCA was launched in 1993, the first satellite to use charge-coupled devices (CCDs) for X-ray astronomy, it became also possible to accurately measure the abundance of other elements in the plasma, such as oxygen, neon, magnesium, silicium, sulphur, calcium and argon [6]. The origin of these elements can be found in the explosions of stars as supernovae, enriching the ICM more and more over time. By measuring the present-day abundances with high accuracy it is possible to determine the ratio between

different types of supernovae [7]. Type Ia supernovae produce high yields in the iron peak, whereas type II supernovae produce mostly α elements, such as Si, S, Ne and Mg [8]. With the high spectral resolution and the large effective area (4650 cm^2 at 1 keV [9]) of XMM-Newton, it recently became possible to constrain different models for supernovae explosion mechanisms (e.g. de Plaa et al. 2007, Sato et al. 2007), but a correct model to fit the obtained abundances perfectly is still to be found.

The object studied here is Abell 4038, a rich cluster of galaxies. It is located in the southern celestial hemisphere, with a right ascension of 23h 47m 43.70s and a declination of -28d 08m 29.4s. It has a redshift of $z = 0.03028 \pm 0.00024$ and the line of sight velocity of it's member galaxies is measured to be $v = 8940 \pm 72$ km/s [10]. When using a Hubble constant of $H_0 = 69.6$ km/s/Mpc, $\Omega_M = 0.286$, $\Omega_\Lambda = 0.714$ and assuming a flat universe [11], the physical scaling for Abell 4038 is 0.610 kpc/arcsecond [12]. The morphology of the cluster can be described by the so-called Bautz-Morgan classification. Developed in 1970 by Laura P. Bautz and William Wilson Morgan, it defines three main types, type I, II and III. Abell 4038 is a type I cluster [13], which means that it is dominated by a bright, large, suppermassive cD galaxy. Furthermore, the X-ray luminosity of the cluster is $4.9 \cdot 10^{43}$ erg s^{-1} [14].

Interesting about Abell 4038 is the presence of a large steep-spectrum radio source located in the clusters central region. The radio source is the result of emission from clouds of relativistic electrons rotating around a magnetic field, evolving over timescales of $\sim$10 million years. The energy loss of these electrons is due to Synchrotron emission, adiabatic expansion and inverse Compton scattering of the cosmic microwave background photons [15]. The projected linear extend of this source is 56 kpc in the north-south direction and the age of the source is estimated to be $6 \cdot 10^7$ years. Such a radio source is called a radio relic, these are diffuse elongated synchotron radio sources with an elongated and irregular form located at the peripheral regions of galaxy clusters. Small radio relics ($<$500 kpc) such as this one are proposed to be fossil lobes of radio plasma produced by active galaxies and revived by shock waves [16]. The spectral index of the source is $\alpha = 2.2 \pm 0.1$, where the spectral index is defined as a measure of the dependence of radiative flux density on frequency as follows [17]:

$$F_\nu \propto \nu^{-\alpha}$$

The shape of the southern part resembles that of a narrow-angle-tail (NAT) source, meaning that all the radio emission lies in a tail on one side of the galaxy and the galaxy itself forms the head of the tail [18]. The problem with this radio relic is that there are no galaxies observed that can be the progenitor for this radio emission. By looking at

Table 1.1. Important information about the cluster: (1) the name, (2) the right ascension, (3) the declination, (4) the redshift, (5) the calculated R_{500} in kpc, (6) the extraction radius for the spectrum in kpc and (7) the scale conversion in kpc per arcsecond.

(1)	**Cluster**	Abell 4038
(2)	**R.A.**	23h 47m 43.7s
(3)	**Dec.**	-28d 08' 29.4"
(4)	z	0.03028
(5)	R_{500} **(kpc)**	854.5
(6)	R_{extr} **(kpc)**	170.9
(7)	**Physical scale (kpc/arcsec)**	0.610

the deep X-ray data of Abell 4038, it may be possible to learn more about this radio relic.

Chapter 2

Methods

2.1 XMM-Newton

The XMM-Newton satellite is the largest scientific satellite ever launched by the ESA, with a length of 10 metres and a weight of 4 tonne. The most important part of the satellite is the X-ray telescope. It consists of three large mirror modules and their associated focal plane instruments. In two of these modules, about half of the incoming light is diverted to two Reflection Grating Spectrometers (RGS) [19], for performing detailed spectral analysis. Besides the X-ray telescopes, XMM-Newton also has a sensitive Optical/UV Monitor Telescope (OM) to perform regular observations of the same field of view as the X-ray telescopes.
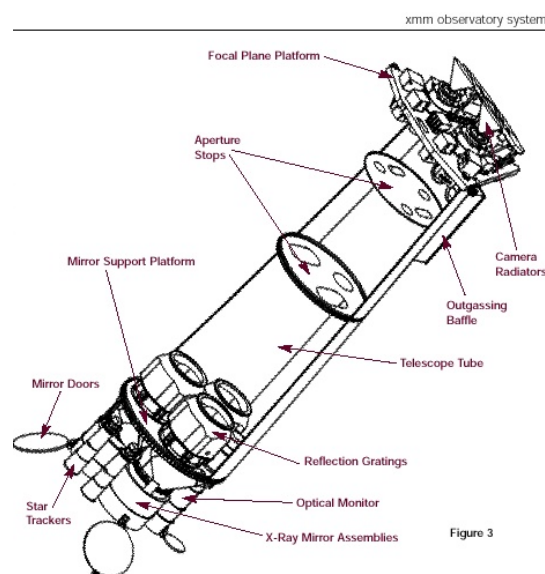

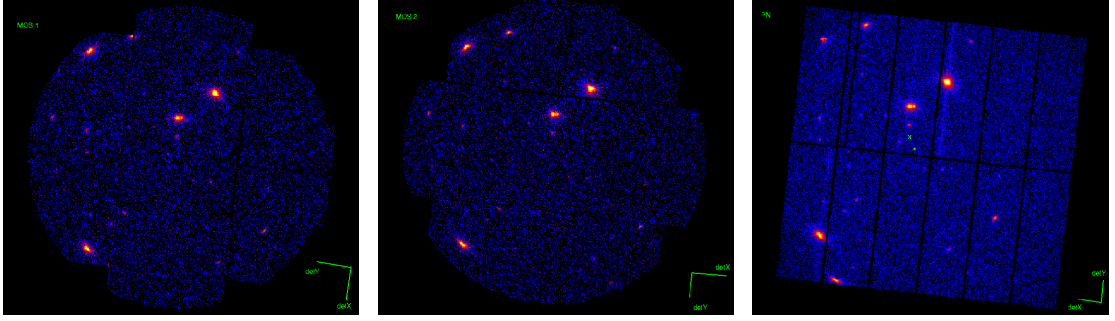**Figure 2.1.** A schematic view of the XMM-Newton sattelite.

Figure 2.2. The field of view for the MOS1 detector (left panel), the MOS2 detector (middle panel) and the PN detector (right panel).

The observations of Abell 4038 were made with the European Photon Imaging Camera (EPIC) onboard of the XMM-Newton satellite. The EPIC consists of three X-ray CCD cameras, two Metal Oxide Semi-conductor (MOS) CCD arrays and one PN camera [9] (see figure 2.2). The PN camera receives an unobstructed beam, while MOS1 and MOS2 receive about 44% of the incoming flux. The angular resolution of the cameras is mostly due to the Point Spread Function (PSF) of the mirror modules. This is because the MOS and PN camera have a pixel size of 40 and 150 micrometer respectively, what corresponds to 1.1" and 4.1" on the sky. The full width at half maximum (FWHM) of the PSF of the mirror modules is around 6", which means that the MOS cameras are fully sampled. The PN camera slightly undersamples the core of the PSF. Furthermore, the spectral resolution of EPIC is $\frac{E}{\Delta E} \sim 20 - 50$. The MOS cameras both have 7 CCD's (10.9 × 10.9 arcminutes), but unfortunately two CCD's in MOS1 are no longer usable due to two micrometeorite impacts scattering debris into the focal plane. The PN camera has 12 CCD's, each 13.6 × 4.4 arcminutes.

During the observation, all three cameras were in full frame mode (MOS) and full extended frame mode (PN), which means that all pixels of all CCD's were read out. The raw exposure time, that is the total time of the observation, is about 66 ks. Due to soft proton flaring some time intervals are to be discarded. Soft proton flares occur when the imaging instruments of the XMM-Newton cross interplanetary clouds of electrically charged particles, where the low energy protons in these clouds are ejected from the sun. When this happens, the count rate of the detectors can increase several orders of magnitude, disturbing the observations. Unfortunately it is not possible to predict when the satellite encounters such clouds, and therefore soft proton flaring can not be prevented [20]. The total time intervals that are eventually used for the data analysis is called the clean exposure time. The raw exposure time and the clean exposure times for the three different cameras are shown in table (2.1).

Table 2.1. Exposure times for the three cameras.

	Raw exposure time (s)	Clean exposure time (s)	Fraction (%)
MOS1	65657	48821.77	74.4
MOS2	65657	49662.20	75.7
pn	61744	44611.21	72.3

2.2 Background in XMM-Newton

The observations that XMM-Newton makes with EPIC have some significant background components to them. Six major contributors will be explained here, starting with the quiescent particle background (QPB).

The quiescent particle background and the fluorescent X-rays

The QPB originates in the penetration of the detector by high energy particles, producing a continuum component, which can be described by a simple, relatively featureless, power law. Often included with the QPB are the fluorescent X-rays (FX). These X-rays come from the interactions between particles and parts of the satellite, before being detected by the detectors. For the MOS detectors, the FX are dominated by the lines Al Kα and Si Kα, with energies of E $\sim$1.49 keV and E $\sim$1.75 keV respectively ([21]). Therefore the FX are the main contributor to the background in the 1.3 - 1.9 keV band, while the QPB is dominant at low energies, below $\sim$1.2 keV, and high energies, above $\sim$2 keV. Because the QPB and the FX are particles that are counted as photons on the detectors, they are not folded trough the instrumental effective area. The lines that are associated with the fluorescent X-rays are listed in table (2.2). The energy of the lines above 2 keV are based on the observations made by D. Iakubovskyi in 2013 [22].

Table 2.2. The instrumental lines for the MOS and PN detectors.

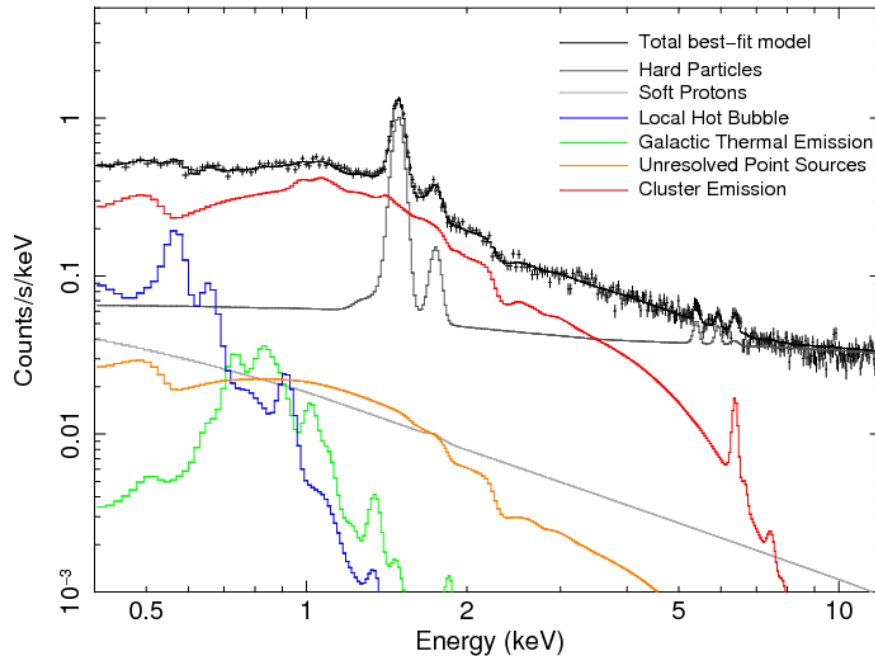| MOS1 and MOS2		PN	
Line	Energy (keV)	Line	Energy (keV)
Al Kα	1.49	Al Kα	1.48
Si Kα	1.75	Ti Kα	4.51
Cr Kα	5.41	Cr Kα	5.42
Mn Kα	5.90	Fe Kα	6.35
Fe Kα	6.40	Ni Kα	7.47
Ni Kα	7.48	Cu Kα	7.98
Zn Kα	8.64	Zn Kα	8.60
Au Kα	9.71	Cu Kβ	8.90
		Zn Kβ	9.57

Figure 2.3. The different background components, taken from Mernier et al. (2014) [23].

The soft-proton background

Besides the QPB and the FX, there is one other background component that is not folded trough the instrumental effective area, the Soft-Proton component (SP). This background comes from low energy protons, usually less than a few 100 keV, ejected from the sun and hitting the detectors. The contribution of this component can vary between undetectable and several orders of magnitude larger than the other contributions. Unfortunately there is nothing to prevent these soft proton flares, and data heavily affected therefore has to be removed for the analysis.

The unresolved point sources

The fourth background component are the unresolved point sources (UPS), with a main contribution from the active galactic nuclei. These AGN are located at the centre of galaxies and are believed to be supermassive black holes accreting mass, resulting in a much higher than normal luminosity. Also galaxies and hot stars have a contribution to the UPS component. The spectral model for the UPS is assumed to be a power-law with a photon index of $\Gamma=1.4$ ([24]). To obtain a constraint for the normalisation of the power-law, the flux of the UPS can be calculated, using the so-called $\log N$-$\log S$ curve (see figure **??**). When this function is integrated, it gives an estimate of the number of point sources in a certain flux range:
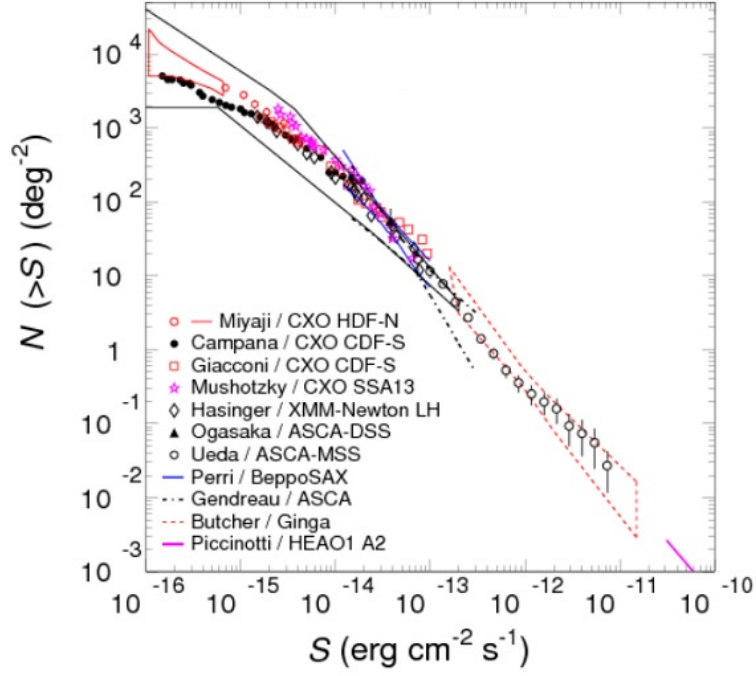
Figure 2.4. The log N-log S curve taken from Kushino et al. 2002 [25]

$$N(< S) = \int_S^\infty \left(\frac{dN'}{dS'} dS' \right) \tag{2.1}$$

Following Lehmer et al. (2012) , the (dN/dS) relations for the different source categories (AGN, galaxies and stars) can be written as:

$$\frac{dN}{dS}^{AGN} = \begin{cases} K^{AGN}(S/S_{ref})^{-\beta_1^{AGN}} & (S \leq f_b^{AGN}) \\ K^{AGN}g\ (S/S_{ref})^{-\beta_2^{AGN}} & (S > f_b^{AGN}) \end{cases} \tag{2.2}$$

where

$$g = (f_b^{AGN}/S_{ref})^{\beta_2^{AGN}-\beta_1^{AGN}}$$

$$\frac{dN}{dS}^{gal} = K^{gal}(S/S_{ref})^{-\beta^{gal}} \tag{2.3}$$

$$\frac{dN}{dS}^{star} = K^{star}(S/S_{ref})^{-\beta^{star}} \tag{2.4}$$

Here, f_b^{AGN} is the flux related to the break in the double power law for the AGN number counts. Furthermore, $S_{ref} = 10^{-14}$ ergs cm^{-2} s^{-1}. In 2006, Hickox et al. measured the flux of the unresolved cosmic x-ray background in the 2-8 keV band to be $(3.4 \pm 1.7) \times 10^{-12}$ ergs cm^{-2} s^{-1} deg^{-2}, based on the Chandra Deep Fields. In the observations

for A4038, the detection limit corresponding to this unresolved flux, 1.4×10^{-13} erg s^{-1} cm^{-2}, is not reached, and therefore the total unresolved flux Ω_{UPS} in the 2-8 keV band can be estimated by:

$$\Omega_{UPS} = 3.4 \times 10^{-12} + \int_{1.4 \times 10^{-13}}^{S_{cut}} S' \left(\frac{dN}{dS'} \right) dS' \tag{2.5}$$

Using equations (2.2), (2.3), (2.4) and the detection limit of the observation for Abell 4038, this total unresolved flux can be easily computed and used to constrain the normalisation of the power law for the UPS background component.

The local hot bubble and Galactic thermal emission

The local hot bubble (LHB) is an irregularly shaped region surrounding the solar system, filled with a hot low-density plasma ($T \sim 10^6$). The radial extent of this halo varies from 30 kpc to over 100 kpc, preferentially out of the direction of the Galactic plane. This background component is dominant at an energy near $\frac{1}{4}$ keV. Because the local hot bubble is directly around our solar system, the X-ray emission from the hot plasma is not absorbed by the column density of the Galactic interstellar medium (ISM), the matter that exists in the space between star systems of our galaxy.

The Galactic thermal emission (GTE) is the emission from the additional hot plasma ($T \sim 10^6$) located in the halo of the Milky Way. This emission is also dominant at energies ≤ 1 keV, and since it is not situated in our immediate surroundings, this component is absorbed by the column density of the Galactic ISM.

2.3   Data reduction

The raw data that comes directly from XMM-Newton has to undergo some procedures to produce a clean image and spectrum, which is done using the software *SAS*[1]. First, we create the event files for MOS and PN, using *emproc* and *epproc* respectively. From these event files the light curves are obtained with *evselect*, an example of such a light curve is shown in figure (2.5). The large peak in the count rate at the left side of the figure is due to soft-proton flaring (see section 2.2). This data can not be used in the analysis and therefore has to be discarded. A good approach to do this, is to look at an histogram of the count rate, as in figure (2.5). The distribution of the count rate is by approximation a Gaussian function near 5.5 counts/s. We now define some sort of
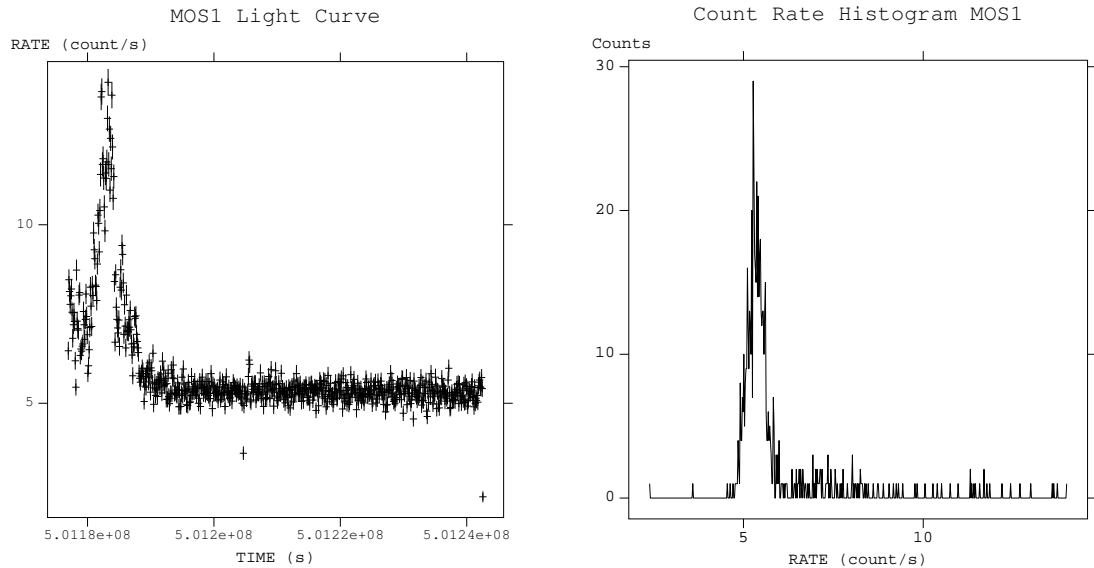
---

[1]http://xmm.esac.esa.int/sas/

Figure 2.5. The lightcurve for MOS1 (left panel), where soft-proton flaring is clearly visible and a histogram of the count rate for MOS1 (right panel), used to determine the good time intervals (GTI).

range, say one sigma (σ) from the centroid of the function, and exclude all the count rates that are not in this range, thus filtering out the bad time intervals.

The next step is creating the images for different energy bands and the corresponding background images, taken from the filter wheel closed (FWC) data. The energy bands used here are 0.3-2 keV, 2-4.5 keV, 4.5-7.5 keV, 7.5-12 keV, 2-8 keV and 10-12 keV. With the PN detector, it is also necessary to remove the so called out-of-time events. This is due to the fact that photons are not only counted during the integration time, but also during the readout of the CCD's, leading to an incorrect energy value. In the observation for Abell 4038, PN was in full extended frame mode, and the fraction of out-of-time events is therefore 2.3 % of all events ([26]). With the task *epproc* and *FTOOLS* we can create an out-of-time event list based on the original data, multiply this list by 0.023 and substract it. After this, the background images are substracted as well from the original images, and the different energy bands are added together to create a total image in the energy range 0.3 to 12 keV.

The obtained total image still needs to be corrected by the exposure maps, which account for the difference in sensitivity of the detectors over their effective area. After normalising these maps such that the highest value is 1, we apply them to the images and obtain the final result shown in figure (2.6).

2.4 Spectrum extraction and analysis

When extracting the spectrum of Abell 4038, we first have to exclude all the point sources. The detection is done with the task *edetect* and a second correction by eye. For the analysis of the core of Abell 4038, the spectrum is extracted in a circle-shaped region around the center of the cluster with a radius of 4.67 arcmin ($0.2 \times R_{500}$, see section 3.1). In figure (2.6) are all the point sources and the core extraction region shown. The redistribution matrix (RMF) and instrument effective area (ARF) are calculated using the commands *rmfgen* and *arfgen* respectively. When all this files are created, a program called *trafo* is used to create the spectra in the right format for the analysis.
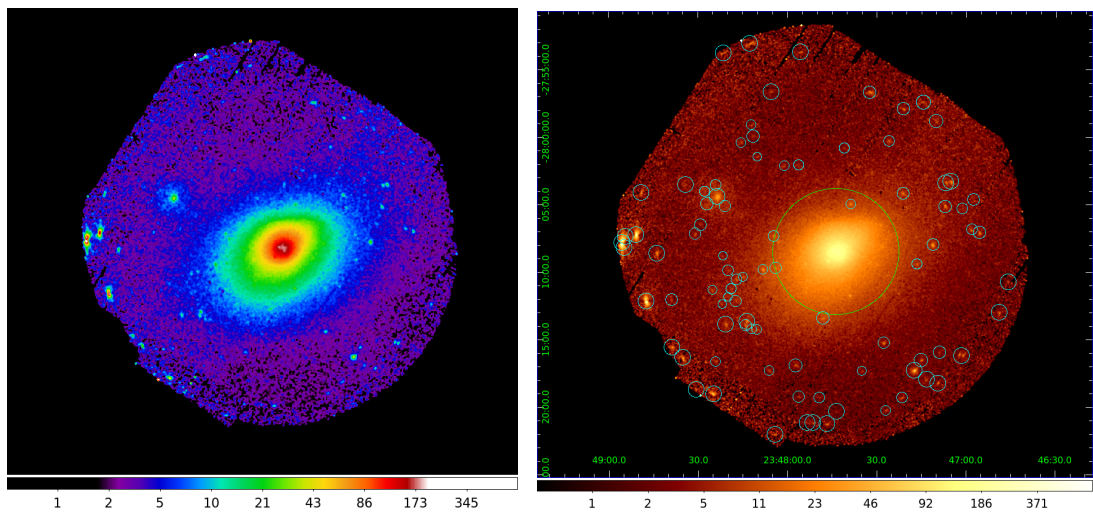

Figure 2.6. The image after the raw data processing in the energy range 0.3 - 12 keV (left panel) and the core extraction region (green) and the point sources that are excluded in the analysis (cyan) (right panel).

For the spectral analysis of Abell 4038 we use the program SPEX [27]. Because EPIC has three instruments, and not all background components are folded trough the instrumental effective area, we first create 6 sectors: Two for every instrument, one folded (sector 1, 3 and 5) and one unaffected (sector 2, 4 and 6) by the ARF file. Here, the sectors 1 and 2 are for MOS1, 3 and 4 for MOS2 and 5 and 6 for PN. For the galactic thermal emission, the local hot bubble and the cluster emission a collisional ionisation equilibrium model (CIE) is used in sector 1, 3 and 5. This model assumes that the plasma is optically thin for its own radiation and that there is no external radiation field that effects the ionisation balance [28]. There are two relevant ionisation processes, of which the first is collisional ionisation. This occurs when a free electron interacts with an atom or ion and transfers part of his energy to a bound electron. This bound electron then has enough energy to escape from it's shell and becomes a free electron. The

second ionisation process is excitation-autoionisation, somewhat similar to collisional ionisation, but with a free electron that has insufficient energy. The bound electron will therefore not escape the ion, but will jump to an excited state. Sometimes, another bound electron will fill the hole left behind by the excited electron, and transfers it's energy to the excited electron, enabling it to escape.

The two recombination processes that play a role here are radiative recombination and dielectronic recombination. Radiative recombination occurs when a free electron is captured by an ion while emitting a photon. Dielectronic recombination is the inverse of excitation-autoionisation, meaning that a free electron is captured by an ion, while a bound electron gets excited to a higher state. Normally this double excited state is not stable, but sometimes one of the excited electrons will fall back trough a radiative transition, creating a stable excited ion.

Altough the CIE model is an isothermal model, it is possible to mimick the effects of non-isothermalilty. This is done by thawing the parameter *sig*, which leads to a Gaussian emission measure distribution defined as:

$$Y(x) = \frac{Y_0}{\sqrt{2\pi}\sigma_T} e^{-(x-x_0)^2/2\sigma_T^2} \tag{2.6}$$

Here Y_0 is the total integrated emission measure, σ_T the width of the distribution, and by default $x \equiv \log T$ and $x_0 \equiv \log T_0$, with T_0 the average temperature of the plasma [29]. The emission measure is also related to the electron density n_e and the hydrogen density n_H by $Y = n_e n_H V$, where V is the volume of the source.

In the same sectors, 1, 3 and 5, we also define a power-law for the unresolved point sources. In sector 2 and 4 a power-law with 8 gaussian lines is used for the quiescent particle background and the fluorescent x-ray instrumental lines. On top of this we use another power-law for the soft-proton background. The same components are added to sector 6, but with one additional gaussian line, as PN has one instrumental line more than the MOS detectors. To take into account the absorption from the column density of the Galactic ISM, an absorption model is created and applied to the GTE, LHB and UPS. For the cluster emission, we compensate for the redshift first using a redshift model and then compensate as well for the absorption.

The first step to fitting the spectrum, is estimating the normalisation for the particle background. To do this, all components, except the QPB, are set to 0 and frozen. Then, only the region from 10 to 12 keV is taken into account, and we fit the spectrum. The values for the obtained normalisations are then frozen. The next step is to add the

Gaussian lines, with the energies shown in table (1). Also the temperature and normalisation of the cluster emission is thawed, and another fit of the spectrum is made. To increase the fit, we thaw the abundances of O, Ne, Mg, Si, S, Ar, Ca, Fe and Ni, while the rest of the abundances are coupled to the abundance of iron. Because the temperature distribution troughout the core region is not assumed to be uniform, the parameter sigma for the cluster emission is also thawed. This means that instead of one peak temperature, a gaussian temperature distribution is obtained.

The correct values for the other background components are now set and the normalisation for the particle background is thawed again to improve the fit some more. Lastly, the full width at half maximum for all the gaussian instrumental lines is thawed, and a final fit is done for the spectrum.

Chapter 3

Results

3.1 Spectrum analysis on the core region

In the analysis on the core region for Abell 4038, we use the energy band from 0.5 to 10 keV and 0.6 to 10 keV for MOS and PN respectively, and a circular region is used with radius $0.2 \times R_{500}$. The radius R_{500} is the radius where the mean enclosed density in the cluster is 500 times the current critical density ρ_c. The following relation has been found for R_{500} by M. Arnaud et al. (2005) [30]:

$$h(z)R_{500} = B_{500} \times \left(\frac{kT}{5 \text{ keV}} \right)^{\beta} \tag{3.1}$$

Since A4038 is at a relatively low redshift, the factor $h(z)$ is approximately equal to 1. The values used for the calculation are $B_{500} = 1104$ kpc, $\beta = 0.57$ and $kT = 3.19$ [31], giving $R_{500} = 854.51$ kpc for A4038. Starting with the spectrum analysis of the $0.2 \times R_{500}$ region with the procedure as described in section (2.4), we obtain the temperature of the cluster core and the most abundant elements.

The observed spectrum with the best-fit spectra for the MOS detectors (blue) and the PN detector (red) are shown in figure (3.1). The results of the analysis of the core region are listed in table (3.1). All the uncertainties are obtained by the command *error* in SPEX and use a 68 % confidence level. The abundance values of each element are all expressed in terms of their ratio with respect to iron. The error propagation is calculated as shown in equation (3.2), where X is an element of our choosing. The abundances are also plotted in figure (3.2), relatively to the abundance of iron.
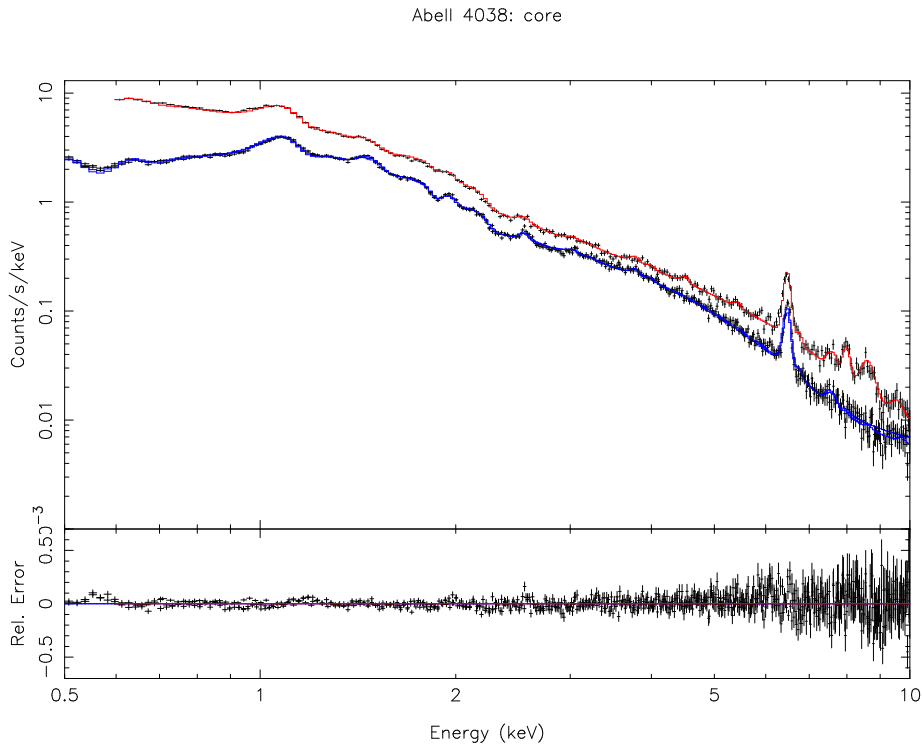
Figure 3.1. The spectrum of the central region of A4038 for MOS and PN, fitted with the background components mentioned in section 2.2 and the cluster emission. The blue (MOS) and red (PN) lines show the best-fit model, respectively.

Table 3.1. The resulting parameters with the best-fit CIE model. The results are derived from the spectral analysis of the core region. For the MOS detector we use the energy band from 0.5 to 10 keV, while for the PN detector we use 0.6 to 10 keV. Here Y is the emission measure and σ_T the width of the gaussian emission measure profile as in equation (2.6).

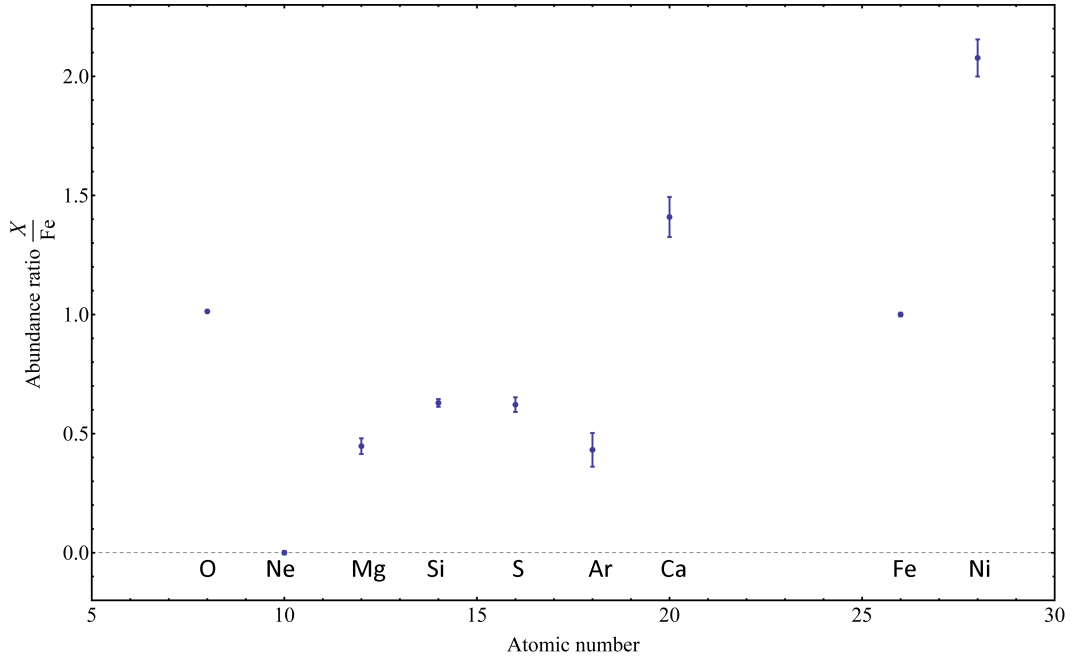| Parameter	Best fit value
χ^2/d.o.f.	1140/759
Y (10^{70} m^{-3})	670.8 ± 2.6
kT (keV)	3.12 ± 0.01
σ_T (keV)	0.235 ± 0.005
O/Fe	1.013 ± 0.002
Ne/Fe	0.000 ± 0.007
Mg/Fe	0.447 ± 0.033
Si/Fe	0.629 ± 0.016
S/Fe	0.622 ± 0.031
Ar/Fe	0.432 ± 0.071
Ca/Fe	1.409 ± 0.084
Fe	0.544 ± 0.008
Ni/Fe	2.077 ± 0.078

Figure 3.2. The abundances relative to iron, obtained from the spectral analysis of the core region. The used energy band is from 0.5 and 0.6 to 10 keV for MOS and PN respectively.

$$\sigma_{\text{new}} = \frac{X}{Fe} \sqrt{\left(\frac{\sigma_X}{X}\right)^2 + \left(\frac{\sigma_{Fe}}{Fe}\right)^2} \tag{3.2}$$

The statistics of this fit are reasonable, but to investigate further improvement, we study the reduces chi-squared when different energy bands are taken into account (see table 3.2). The fit clearly improves when the lower energy band is discarded, especially in the range 0.5 - 1.5 keV. This may come from incorrect calibration of the contamination on the detectors in the lower energy range. Unfortunately, if we exclude this range for the spectral analysis, we loose essential data, and therefore the energy bands are not changed.

Table 3.2. The reduced chi-squared for the best model fit when different energy bands are taken into account.

Energy band MOS (keV)		Energy band PN (keV)		χ^2/ d.o.f.	χ^2_{red}
Low	*High*	*Low*	*High*		
0.5	10	0.6	10	1140/759	1.50
1.0	10	1.0	10	919/672	1.37
1.5	10	1.5	10	718/598	1.20
0.6	9	0.6	9	1079/699	1.54
1.0	9	1.0	9	882/624	1.41
1.5	9	1.5	9	677/551	1.23

In 2007, de Plaa et al. [7] measured the temperatures and abundances for 22 different

clusters of galaxies. For the comparison of these results with our results, they are overplot with each of the abundances that we obtained with respect to the mean temperature (see figure 3.3). Most element abundances are consistent with the other clusters of galaxies, but the abundance of nickel is slightly higher than average.
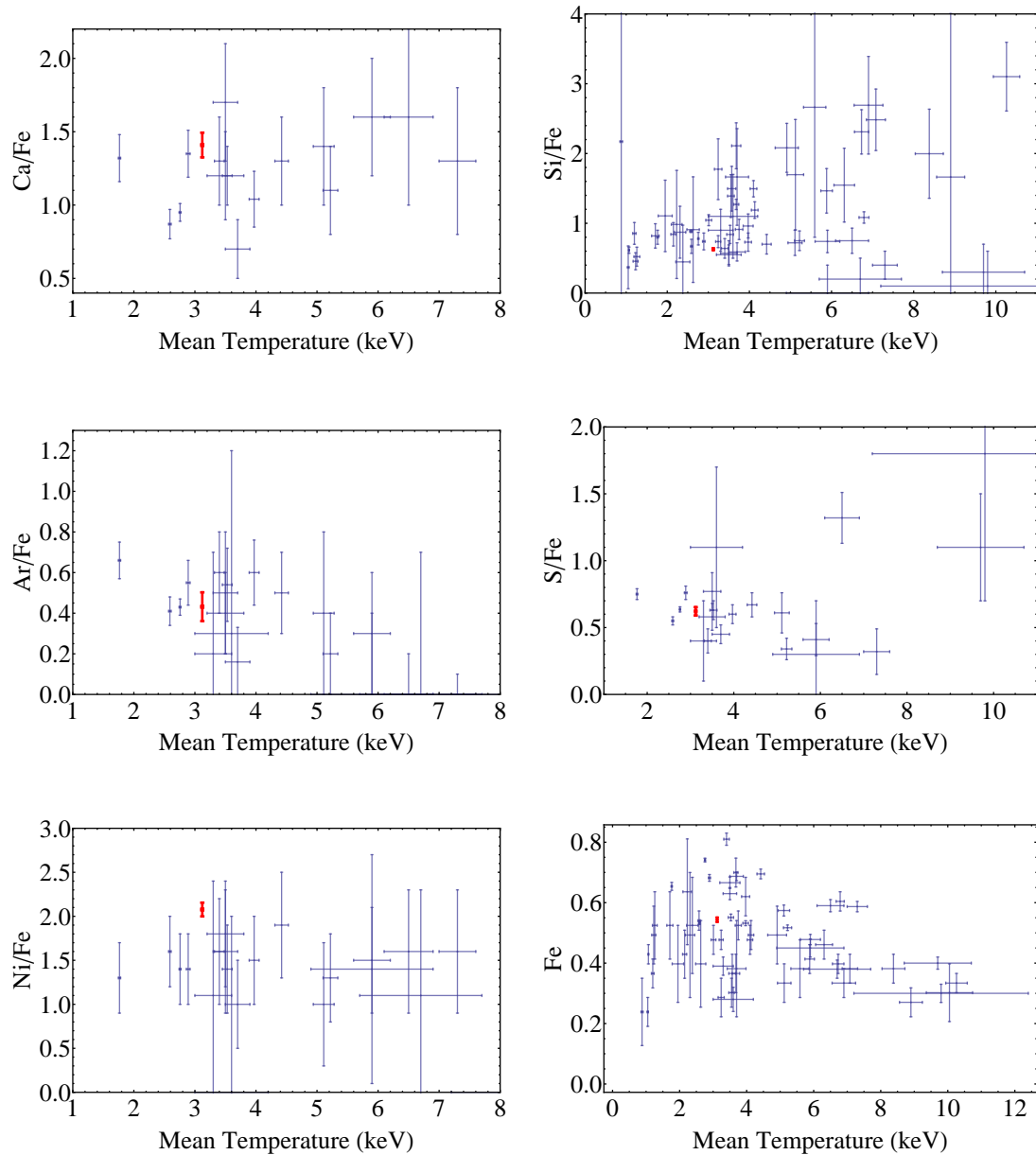

Figure 3.3. The abundances obtained from the spectral analysis of the core (in red), overplot with the results of de Plaa et al. (2007) for different clusters (in blue).

3.2 Radial analysis

To investigate the radial distribution of the ICM temperature and abundances we have applied the same analysis as for the core region to concentric annuli. Therefore the spectra of 7 annular regions with boundaries at 0', 0.6', 1.2', 1.8', 2.4', 3', 4.75' and 6' centered on R.A.= 23h 47m 43.70s and δ= -28d 08m 29.4s are extracted (see figure **??**. Six of these spectra are shown in figure (3.4) with the best-fit model for the MOS and PN detectors in red. The obtained temperature and reduced chi-squared for each annulus are shown in table (3.3), and the temperature profile is plotted as well in figure (3.5). The uncertainties in the radius are just the radii of the annuli. Apart from the annulus from 2.4' to 3', the temperature profile shows a clear indication for the presence of cooler plasma in the inner core of the cluster, and higher temperatures when further away from the inner core. At sufficient radius, the temperature of the plasma decreases again, as the density is also lower there. This follows from the radial profile surface brightness in figure (4.2*b*), which is related to the electron density squared. When trying to obtain a spectral fit of annuli further away than 6.5 arcminutes, the quality of the fitting decreased and the reduced chi-squared became so large that these results were not significant anymore.

From the same analysis, the radial profile of the iron abundance and the silicium abundance are obtained and plotted in figure (3.6). Both results show a peak abundance towards the center of the cluster and a little bump at around 2 arcminutes.

Table 3.3. The outcome for the best fit model using a CIE model. The results are derived from the spectral analysis of the core region. For MOS we use the energy band from 0.5 to 10 keV, while for PN we use 0.6 to 10 keV.

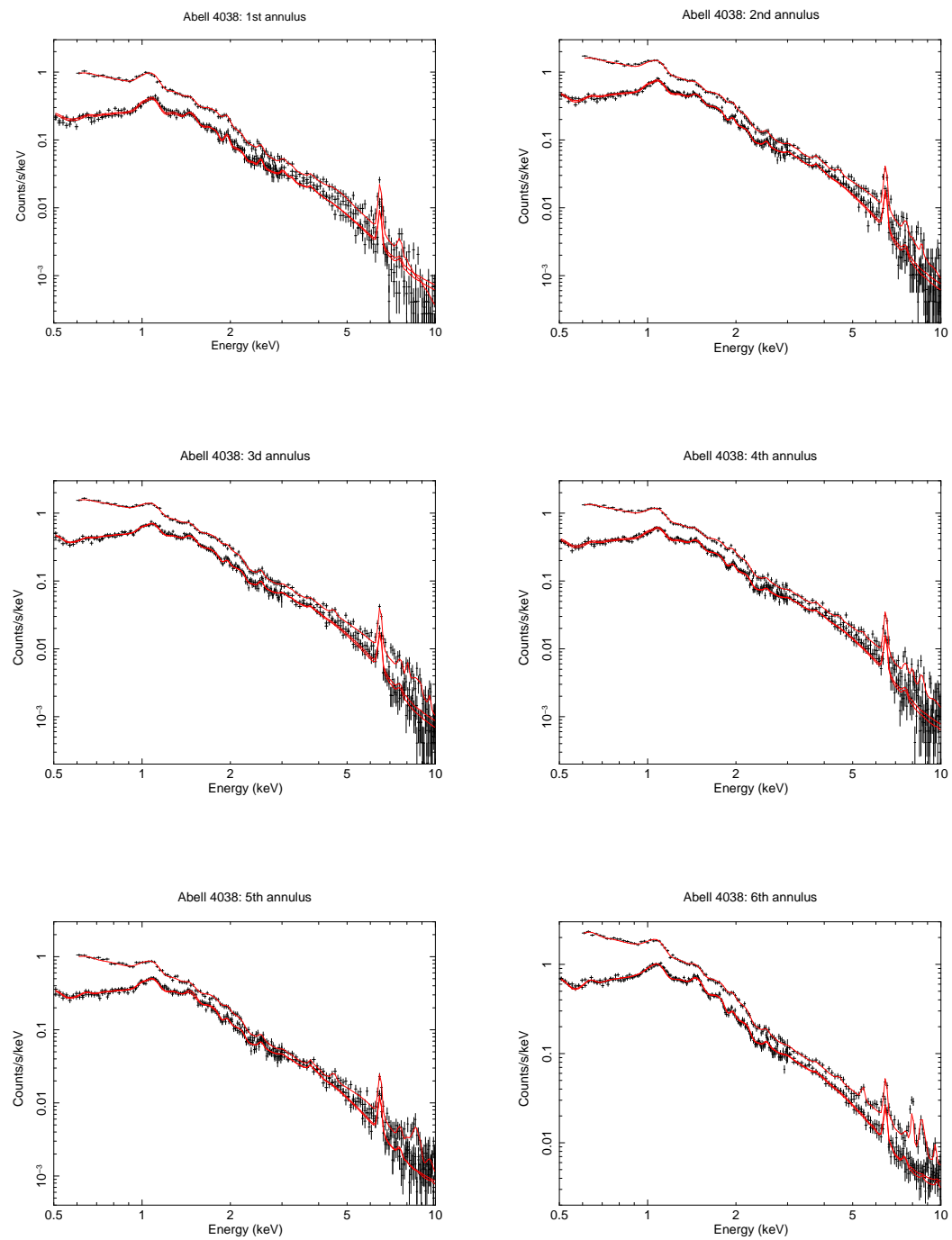| Radius (arcmin)		χ^2/d.o.f.	kT (keV)
From	*To*		
0	0.6	992/650	2.60 ± 0.03
0.6	1.2	840/659	2.91 ± 0.03
1.2	1.8	825/659	3.03 ± 0.02
1.8	2.4	755/655	3.04 ± 0.03
2.4	3	721/647	2.96 ± 0.04
3	4.75	916/698	3.06 ± 0.02
4.75	6.5	909/677	2.77 ± 0.05

Figure 3.4. The observed spectra (black) with the best fit model (red) for the six concentric annuli. The energy bands are from 0.5 and 0.6 to 10 keV for MOS and PN respectively.
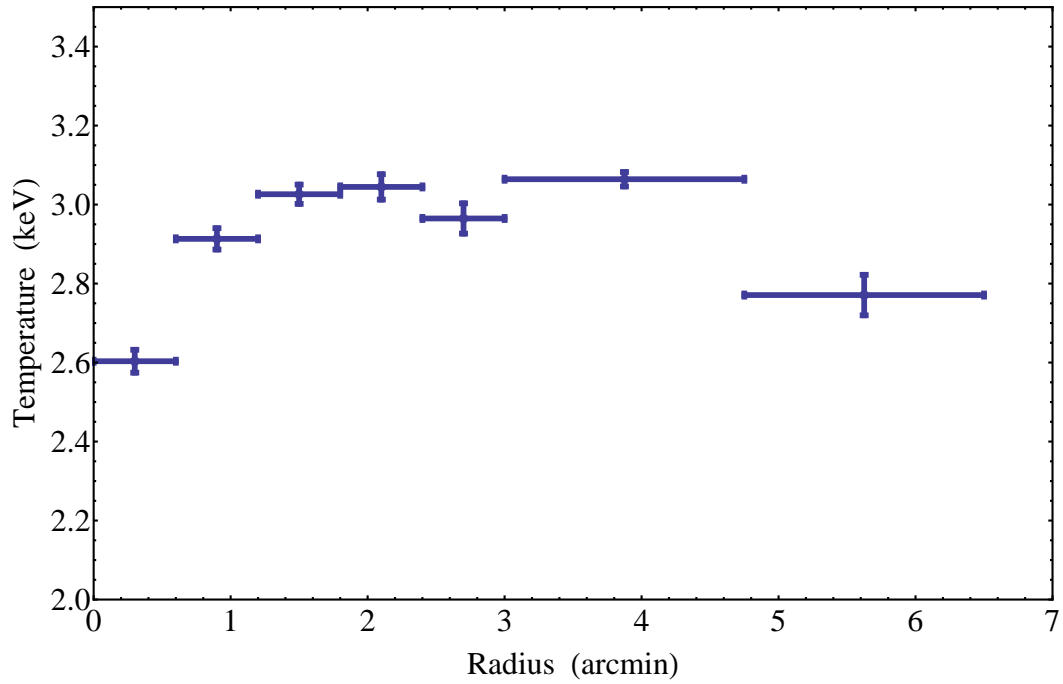
Figure 3.5. The temperature profile for Abell 4038, obtained from the spectral analysis of seven concentric annuli.
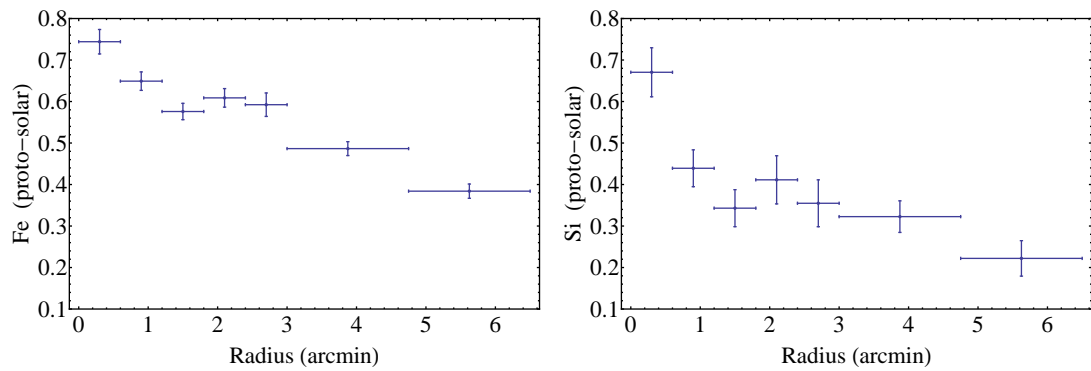

Figure 3.6. A plot of the radial profile of the iron (left panel) and silicium (right panel) abundances. The abundances are relative to the proto-Solar abundances of Lodders et al. (2009).

3.3 Hardness Ratio

The hardness ratio is a frequently used measure to quantify and characterize the source spectrum. This ratio compares two bands in the X-ray, often the hard passband (H) and the soft passband (S) [32]. There are multiple definitions for the hardness ratio, some more convenient than others, but the one that will be used here is the simple form:

$$\mathcal{R} = \frac{H}{S} \tag{3.3}$$

The energy bands for the calculation are 0.3 - 2 keV for the soft band and 2 - 4.5 keV and 4.5 - 7.5 keV for the hard band, resulting in hardness ratio plots as in figure (3.7). For clarity purposes the images are binned with a factor of 8 pixels and also smoothed with a Gaussian function with a radius of 4 pixels.
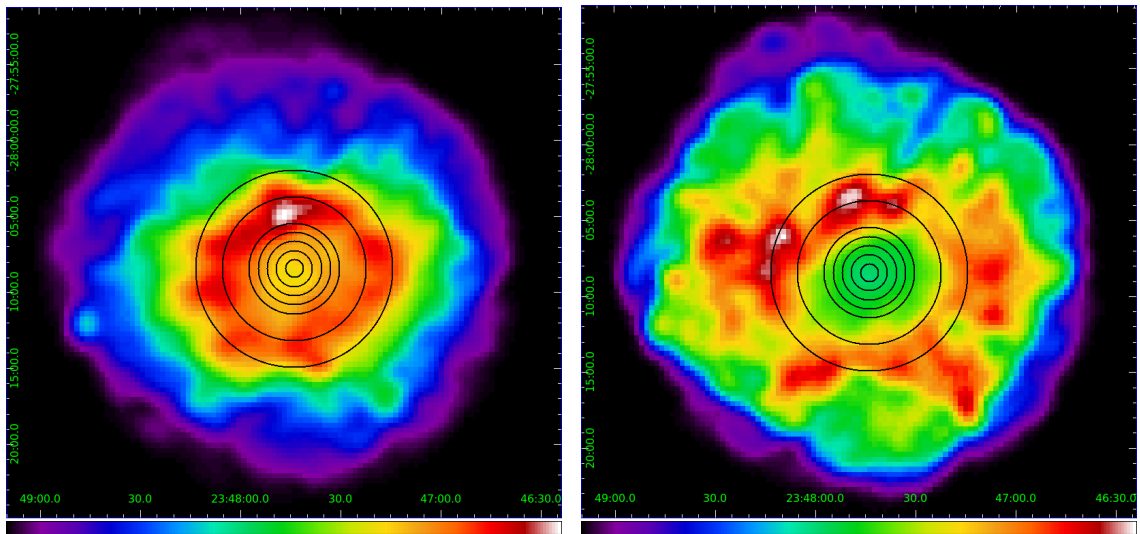

Figure 3.7. A plot of the hardness ratio using 0.3 - 2.0 keV for the soft energy band and 2.0 - 4.5 keV (left panel) and 4.5 - 7.5 keV (right panel) for the hard energy band. The images are binned with a factor of 8 pixels and smoothed with a Gaussian function with a 4 pixel radius.

3.4 Radial profile surface brightness

It is also instructive to make a radial profile of the surface brightness of the cluster. Such a radial profile is made by taking a region and calculate the linear projection of the intensity at different radii. We have done this for 4 regions, shown in figure (3.8). Region I is a pie-shaped region in the opposite direction of the radio relic in Abell 4038, whereas region II is a pie-shaped region in the direction of the relic. Region III is a

circular region to obtain a total radial profile of the surface brightness, and region IV is a small region to investigate the surface brightness closer to the relic. The energy range for all these radial profiles is from 0.3 to 12 keV, and one in the lower energy range from 0.3 to 2 keV for region II. These four different datasets, with the exception of the zoomed in region at the relic, are all fitted with a Beta-model, which is defined in equation (3.4). The obtained values for β, S_0 and r_c are shown in table (3.4).

$$S(R) = S_0 \left(1 + \left(\frac{R}{r_c} \right)^2 \right)^{0.5 - 3\beta} \tag{3.4}$$
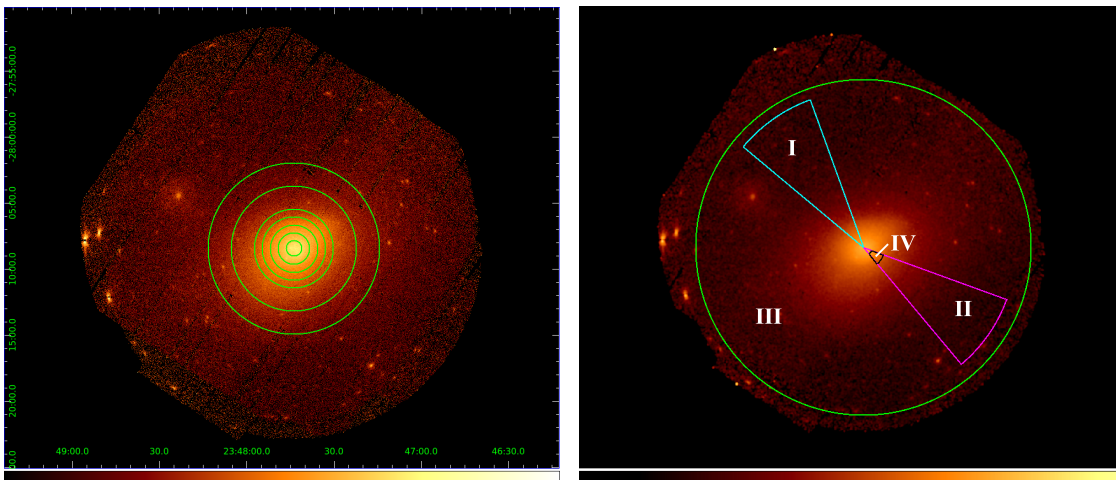

Figure 3.8. On the left panel the concentric annuli used for the radial spectral extraction and analysis and on the right panel the regions taken for the radial profiles of the surface brightness.

Table 3.4. The outcomes for the Beta-model used on different regions: a pie shaped region in the direction of the radio relic in the energyband 0.3-2.0 keV (a) and in the range 0.3-12 keV (b), a pie shaped region in the opposite direction of the radio relic in the range 0.3-12 keV (c) and a circle around the centre in the range 0.3-12 keV (d).

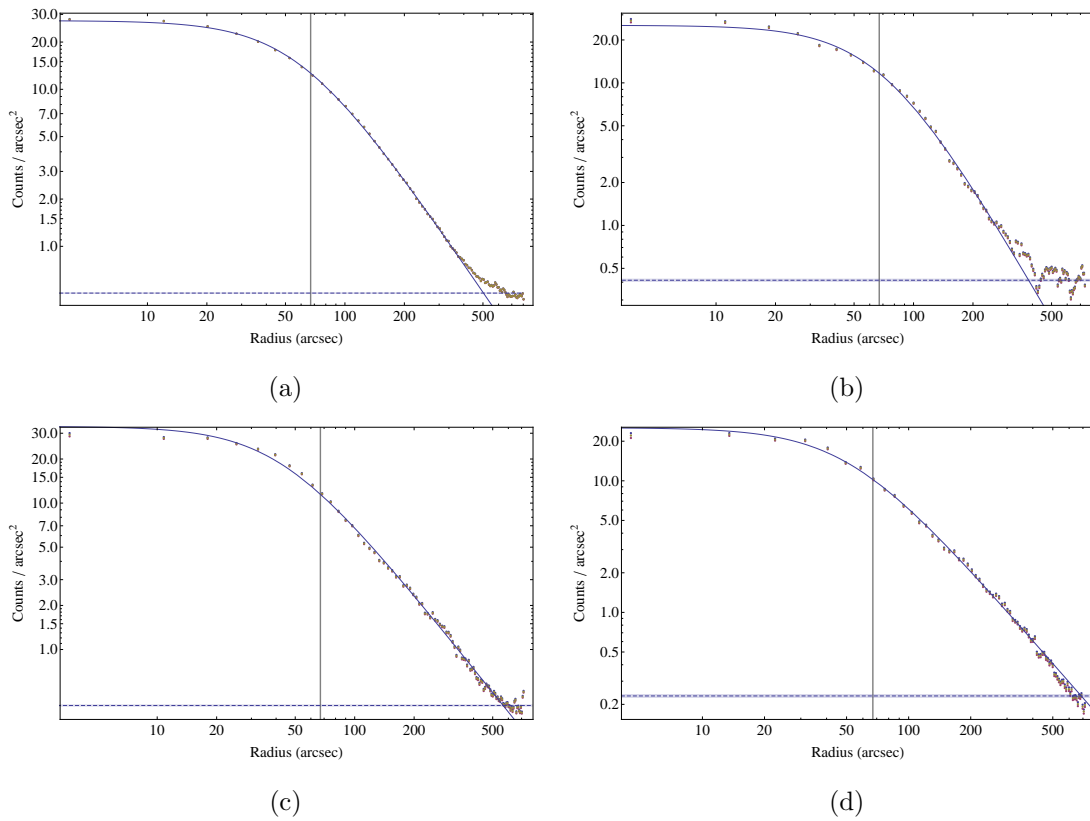|	S_0	r_c (arcsec)	β	χ^2_{red}	d.o.f.	r_{model}
(a)	24.6 ± 0.8	54.5 ± 1.8	0.478 ± 0.004	2.07	3	600
(b)	33.3 ± 1.1	42.5 ± 1.6	0.450 ± 0.004	5.47	3	400
(c)	25.4 ± 0.8	69.8 ± 2.9	0.565 ± 0.011	6.10	3	300
(d)	27.5 ± 0.2	58.3 ± 0.6	0.474 ± 0.001	5.95	3	400

(a)

(b)

(c)

(d)

Figure 3.9. The radial profiles of the surface brightness for different regions are shown here, with a Beta-model fitted trough the data. The blue dashed line is the background noise and the grey vertical line is the position of the radio relic. The four different regions are annuli around the whole cluster (a), a pie-shape in the opposite direction of the relic (b), a pie-shape in the direction of the relic for the whole energy band (c) and for 0.3 - 2 keV (d).

Chapter 4

Discussion

4.1 Abundances

Through measuring the element abundances, the enrichment in the ICM can be studied in detail. The abundances obtained by the spectral fitting of the cluster core are shown in table (3.1). Notable is the seemingly zero abundance of neon. This is probably because of the fact that the neon emission lines have an energy of 1.02 keV, which is just slightly higher than the center of the Fe-L complex. The spectral resolution of XMM-Newtons EPIC detectors ($E/\Delta E \sim 20$ - 50) is insufficient to resolve the different lines in this complex, making the abundance of neon very sensitive to uncertainties in the temperature modeling [4].

All the abundances, with the exception of oxygen, neon and magnesium, are compared with the results of spectral analysis of 22 other clusters, reported by de Plaa et al. (2007)

Table 4.1. Comparison of the ration between type Ia (SNIa) and core collapse supernova (SNcc) when different models are used. Here (1) shows our results, (2) the results by de Plaa et al. 2007, (3) the results by Mernier et al. 2014 and (4) the result of Sato et al. 2007.

SNcc model	SNIa model	(1)	(2)	(3)	(4)
Salpeter IMF Z=0.02	Tycho	0.45 ± 0.09	0.44 ± 0.05	0.37 ± 0.06	-
Salpeter IMF Z=0.02	WDD2	0.52 ± 0.10	0.37 ± 0.09	0.37 ± 0.06	0.28 ± 0.15
Top-heavy IMF Z=0.001	Tycho	0.68 ± 0.06	0.62 ± 0.04	0.56 ± 0.04	-

Table 4.2. The element yields for different supernoave models. The values are given relative to the proto-Solar abundances of Lodders et al. (2009)

	SNIa		SNcc	
	WDD2	*Tycho*	*Salpeter IMF* *Z=0.02*	*Top-heavy IMF* *Z=0.001*
O	0.066	0.12	1.57	3.564
Ne	0.001	0	0.48	0.642
Mg	0.005	0	0.14	0.269
Si	0.207	0.17	0.126	0.267
S	0.124	0.13	0.054	0.107
Ar	0.025	0.03	0.009	0.016
Ca	0.024	0.04	0.007	0.013
Fe	0.792	0.8	0.093	0.076
Ni	0.059	0.05	0.004	0.002

[7]. The elements Ca, Si, S, Ar, and Fe are consistent with the other observed clusters. The abundance of nickel however seems to be a little overestimated. A possible explanation is that the nickel lines are too much dominated by the background noise. The most prominent lines of nickel lie around 7.5 keV [33], where the hard particle background becomes a significantly more important part of the spectrum. This is also illustrated in figure (3.1), where one can see that the relative error of the fit becomes increasingly larger at higher energies. The consistency of the abundances with other clusters suggest that the enrichment history of the ICM in clusters is more or less similar. Below we calculate the supernovae ratio responsible for this enrichment.

As described in chapter 1, it is possible to estimate the contributions from supernovae type Ia (SNIa) and core collapse supernovae (SNcc) from the abundances. The element yields for different models of supernovae are shown in table (4.2), and with these different models a fit is made to obtain the ratio between type Ia and core collapse supernovae. Because the abundances of oxygen, neon and magnesium are a bit uncertain, these are not taken into account when fitting the model. Also the abundance of nickel is discarded, as it is not consistent with other data. Two of the best results are shown in figure (4.1). The first fit uses the yields of the supernova Tycho by Badenes et al. (2009) as a type Ia supernova and a core collapse model with progenitor metallicity $Z = 0.02$ integrated over a Salpeter IMF (initial mass function) , resulting in a ratio $SNIa/(SNIa + SNcc) = 0.45 \pm 0.09$ with $\chi^2/$d.o.f. $= 15/3$. The second fit also uses the Tycho results, but a core collapse model with progenitor metallicity $Z = 0.001$ integrated over a top-heavy IMF. This results in a ratio of 0.68 ± 0.06 with $\chi^2/$d.o.f. $= 14/3$. This values are compared with the results from de Plaa et al. (2007), who obtained a ratio of 0.44 ± 0.05 for the core collapse model with $Z = 0.02$ progenitor metallicity integrated over a Salpeter IMF.

For the Z = 0.001 progenitor metallicity integrated over a top-heavy IMF they obtained a ratio of 0.62 ± 0.04. Both of these values are consistent with the values obtained with our fits. Furthermore the value of the ratio with a WDD2 model (delayed detonation model from Nomoto et al. 1997b [34]) and a Salpeter IMF with Z=0.02 is compared with the value found by Sato et al. 2007 [35], 0.28 ± 0.15. The ratio we obtained, 0.52 ± 0.10, is significantly higher. This is possibly due to the neglection of oxygen and neon in the fit, which are mainly produced in core collapse supernovae, thus overestimating the type Ia contribution. The same overestimation is seen with respect to the ratio's found by Mernier et al. 2014 [23] (see table 4.1).
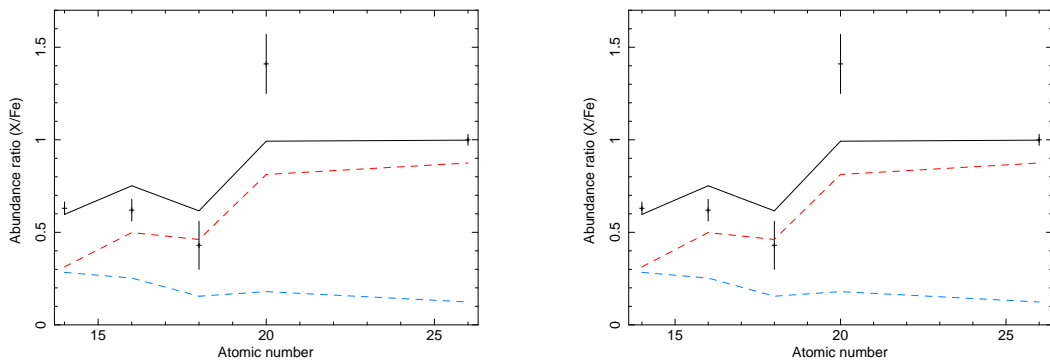

Figure 4.1. Fits using the yields of the supernova Tycho for SNIa and SNcc yields for progenitors metallicity Z=0.02 integrated over a Salpeter IMF (left panel) and SNcc yields for progenitors metallicity Z=0.001 integrated over a top-heavy IMF (right panel). The red dashed line is the SNIa contribution, the blue dashed line the SNcc contribution and the black line is the total fit.

When looking at the radial profiles of the abundance of silicium and iron, they both show a peak towards the center of the cluster. These profiles are compared with the results of Sato et al. 2009, Tokoi et al. 2008, Matsushita et al. 2007 and Mernier et al. 2014 in figure (4.2). They all show a similar trend of a peak towards the center, but the profiles seem a bit steeper. One explanation for this is the fact that for some of the papers instead of R_{200}, R_{180} was used, leading to horizontal compression with respect to our results. Furthermore, the results would be significantly more similar to other clusters when the trend of the first three data points would be extrapolated. Instead there is some sort of increase in abundance at around $0.15\ R/R_{200}$, which might be due to an error in the spectrum analysis.

The centrally peaked abundances of iron and silicium suggest that Abell 4038 is a relaxed cluster. Non-relaxed clusters tend to show more flattened out radial abundance profiles, because there is more mixture of the gas.
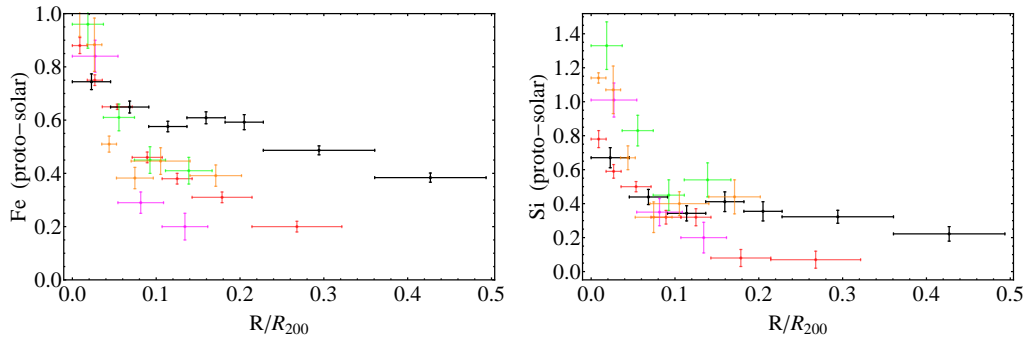
Figure 4.2. Comparison of the radial profiles of iron (left panel) and silicium (right panel). The results for Abell 4038 are shown in black, the other results are taken from Mernier et al. 2014 (red), Sato et al. 2009 (green), Tokoi et al. 2008 (magenta) and Matsushita et al. 2007 (orange).

4.2 Temperature Profile

The obtained radial temperature profile of Abell 4038 shows that towards the center of this cluster the temperature drops significantly, leading to the indication that it is a so called Cool-Core cluster (CC cluster). There is still an ongoing debate on how the mechanisms behind this cooling works. It was first believed that, because of the high density in the core of these clusters, the radiative cooling time would be shortest here [36]. Because of the lower temperature, the pressure to support the overlaying gas has to rise, and the only way of achieving this is for the gas to flow inwards, creating a cooling flow. This theory assumes that there is no other heating mechanism in the center of the cluster, other than gas flow. In 2001, Peterson et al. [37] discovered a lack of emission lines in the 1-2 keV range, which would be expected in the presence of cool gas. This indicates that something is preventing the gas to cool down any further. A reasonable solution is that the cool gas is being heated by AGN outbursts, as discussed by McNamara et al. (2005) [38].

For Abell 4038, a similar result follows from the hardness ratios, shown in figure (3.7). For comparison with the temperature profile, the annuli for which the spectra are extracted are overplotted on the hardness ratios. As most of the X-ray emission in the cluster is through thermal brehmsstrahlung radiation, it can be shown that the hardness ratio is indeed an indicator for temperature. The X-ray luminosity (S_x) for brehmsstrahlung is given by:

$$S_x \propto \int_{E_1}^{E_2} n_e^2 T^{-1/2} e^{-E/kT} G(E,T) dE \tag{4.1}$$
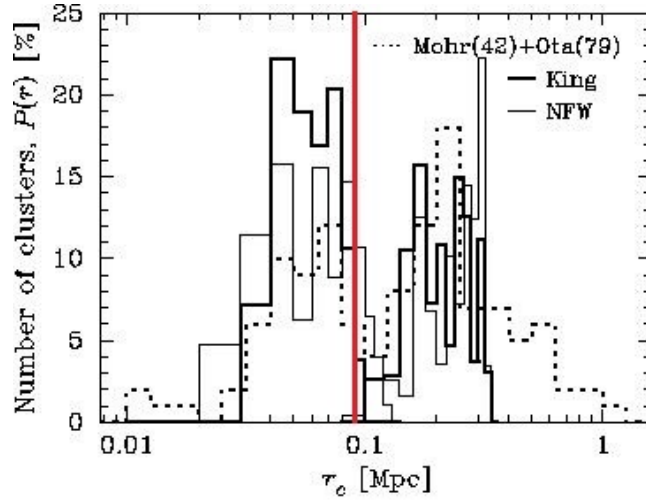
Figure 4.3. The distribution of r_c values from 121 clusters (dotted line) taken from Akahori et al. 2006. The red line is the resultant r_c for Abell 4038.

Here, $E_1 - E_2$ is the energy band, $G(E, T)$ is the quantum correction Gaunt factor and n_e is the electron number density [39]. The hardness ratio is simply S_{x2}/S_{x1}, which after integration is roughly proportional to $(T_2/T_1)^{1/2}$, meaning that a higher hardness ratio is a result of more hard X-ray emission, indicating higher temperatures. By looking at the hardness ratio, one can see that the increase in the hardness ratio when moving radially away from the cluster core approximately corresponds to the temperature profile in figure (3.5).

4.3 Morphology

By looking at the radial profile of the surface brightness the morphology of Abell 4038 can be discussed. The different values of r_c, the core radius, for the four regions show that the cluster is not perfectly symmetrical. The large value of r_c in the north-east direction suggests that the core region is somewhat stretched here. Looking at the hardness ratio, we see that in the north-east direction this ratio is also somewhat higher, indicating a higher temperature. It is possible that these two results are correlated, but with the data available a definite conclusion can not be made.

The obtained r_c value for Abell 4038 is compared to the values of 121 other clusters in figure (4.3). Our result lies in the left peak, indicating again a relaxed cluster, while larger values of r_c indicate a merging cluster. This is because when a merger takes place, the gas could form a large, flat core [40].

4.4   conclusion

From an X-ray observation with XMM-Newton the cluster Abell 4038 has been studied and analysed. The abundances in the intracluster medium are obtained and do not vary significantly from other clusters, indicating a similar enrichment history. From these abundances the ratio of supernovae type Ia and core collapse supernovae is calculated. The current models still do not provide an acceptable fit of the element abundances, especially the high calcium abundance is underestimated. The radial temperature profile shows that A4038 is a cool-core cluster, and the radial profile of iron and silicium, together with the obtained r_c value indicate that the cluster is relaxed. Unfortunately, the analysis of this observation is insufficient to obtain results about the radio relic discussed in section 1.

Bibliography

[1] L. Feretti. Clusters of galaxies: observational properties of the diffuse radio emission. *The Astronomy and Astrophysics Review*, 2012.

[2] J. R. Peterson and A. C. Fabian. X-ray spectroscopy of cooling clusters. *Physics Reports*, 2006.

[3] A. V. Kravtsov and S. Borgani. Formation of galaxy clusters. *Annual Reviews of Astronomy & Astrophysics*, 2012.

[4] H. Bohringer and N. Werner. X-ray spectroscopy of galaxy clusters. *The Astronomy and Astrophysics Review*, 2009.

[5] R. J. Mitchell. Ariel 5 observations of the x-ray spectrum of the perseus cluster. *Mon. Not. R. Astron. Soc.*, 1976.

[6] R. Mushotzky. Measurement of the elemental abundances in four rich clusters of galaxies. *ApJ*, 1996.

[7] J. de Plaa. Constraining supernova models using the hot gas in clusters of galaxies. *A&A*, 2007.

[8] W. H. Baumgartner. Intermediate-element abundances in galaxy clusters. *ApJ*, 2004.

[9] XMM-Newton Community Support Team. Xmm-newton users handbook.

[10] R. de Propris and W. J. Couch. The 2df galaxy redshift survey: a targeted study of catalogued clusters of galaxies. *Mon. Not. R. Astron. Soc.*, 2002.

[11] Planck Collaboration. Planck 2013 results. xvi. cosmological parameters. *A&A*, 2014.

[12] E. L. Wright. A cosmology calculator for the world wide web. *Publ. Astron. Soc. Pac.*, 2006.

[13] O. B. Slee and A. L. Roy. An extreme example of a radio relic in abell 4038. *Mon. Not. R. Astron. Soc.*, 1998.

[14] T. H. Reiprich and H. Bohringer. The mass function of an x-ray flux-limited sample of galaxy clusters. *ApJ*, 2002.

[15] R. Kale and K. S. Dwarakanath. Multi-frequency studies of radio relics in the galaxy clusters a4038, a1664, and a786. *ApJ*, 2012.

[16] T. A. Ensslin and M. Bruggen. On the formation of cluster radio relics. *Mon. Not. R. Astron. Soc.*, 2002.

[17] B. W. Carroll and D. A. Ostlie. *An Introduction to Modern Astrophysics.* Pearson, 2001.

[18] C. L. Sarazin. *X-ray Emission From Clusters of Galaxies.* Cambridge University Press, 1988.

[19] J. W. den Herder and A. C. Brinkman. The reflection grating spectrometer on board xmm-newton. *A&A*, 2001.

[20] J. Pradas and J. Kerp. Xmm-newton data processing for faint diffuse emission. *A&A*, 2005.

[21] S. L. Snowden. Cookbook for analysis procedures for xmm-newton epic observations for extended objects and the diffuse background, 2014.

[22] D. Iakubovsky. *Constraining properties of dark matter particles using astrophysical data.* PhD thesis, Leiden University, 2013.

[23] F. Mernier. Abundance and temperature distributions in the hot intra-cluster gas of abell 4059. *A&A*, 2014.

[24] A. de Luca. The 2-8 kev cosmic x-ray background spectrum as observed with xmm-newton. *A&A*, 2003.

[25] A. Kushino. Study of the x-ray background spectrum and it's large-scale fluctuation with asca. *Publ. Astron. Soc. Japan*, 2002.

[26] I. de la Calle. *Users Guide to the XMM-Newton Science Analysis System*, 2014.

[27] J. Kaastra and R. Mewe & H. Nieuwenhuijzen. Spex: a new code for spectral analysis of x & uv spectra, 1996.

[28] J. Kaastra. Thermal radiation processes. *Space Science Reviews*, 2008.

[29] J. Kaastra. *SPEX manual*, 2014.

[30] M. Arnaud, E. Pointecouteau, and G. W. Pratt. The structural and scaling properties of nearby galaxy clusters. *A&A*, 2005.

[31] K. A. Frank. Characterization of intracluster medium temperature distributions of 62 galaxy clusters with xmm-newton. *ApJ*, 2013.

[32] T. Park. Bayesian estimation of hardness ratio: modeling and computations. *ApJ*, 2006.

[33] J. Kaastra. *Line list SPEX version 2.0*, 2001.

[34] K. Nomoto. Nucleosynthesis in type ia supernovae. *Nuclear Physics A*, 1997.

[35] K. Sato. Type ia and ii supernovae contributions to metal enrichment in the intracluster medium observed with suzaku. *ApJ*, 2007.

[36] A. C. Fabian. Cooling flows in clusters of galaxies. *Annual Reviews of Astronomy & Astrophysics*, 1994.

[37] J. R. Peterson. X-ray spectroscopy of the cluster of galaxies abell 1795 with xmm-newton. *A&A*, 2001.

[38] B. R. McNamara. The cluster-scale agn outburst in hydra a. *ApJ*, 2005.

[39] J. A. Peacock. *Cosmological Physics*.

[40] T. Akahori. Core structure of intracluster gas: effects of radiative cooling on core sizes. *Publ. Astron. Soc. Japan*, 2006.